A Multiresolution Model for Small-Body Gravity Estimation

**Brandon A. Jones · Gregory Beylkin ·
George H. Born · Robert S. Provence**

Abstract A new model, dubbed the MRQSphere, provides a multiresolution representation of the gravity field designed for its estimation. The multiresolution representation uses an approximation via Gaussians of the solution of the Laplace's equation in the exterior of a sphere. Also, instead of the spherical harmonics, variations in the angular variables are modeled by a set of functions constructed using quadratures for the sphere invariant under the icosahedral group. When combined, these tools specify the spatial resolution of the gravity field as a function of altitude and required accuracy. We define this model, and apply it to representing and estimating the gravity field of the asteroid 433 Eros. We verified that a MRQSphere model derived directly from the true spherical harmonics gravity model satisfies the user defined precision. We also use the MRQSphere model to estimate the gravity field of Eros for a simulated satellite mission, yielding a solution with accuracy only limited by measurement errors and their spatial distribution.

1 Introduction

In this paper, we develop a new approach to estimating the gravity field of a small body by introducing a multiresolution representation of the gravity potential. In

B. A. Jones and G. H. Born
Colorado Center for Astrodynamics Research
University of Colorado, UCB 431
Boulder, CO, 80309, USA
Tel: +1303-735-4490
E-mail: jonesba@colorado.edu

G. Beylkin
Department of Applied Mathematics
University of Colorado, UCB 526
Boulder, CO, 80309, USA

R. S. Provence
Aerosciences and Flight Mechanics Division
NASA Johnson Space Center
2101 NASA Parkway
Houston,TX, 77058, USA

addition, instead of the spherical harmonics, we model variations in the angular directions by an alternate set of functions constructed using quadratures for the sphere invariant under the icosahedral group. This paper presents an initial proof of concept to unweave the estimation problem from its current reliance on the spherical harmonics and the expansion of the gravity potential via the inverse powers of the radial variable.

When estimating the gravity field of a primary body, it is important to stage the estimation in a natural manner. In such a procedure, one would like to first obtain the low spatial frequencies of the model and, then, gradually higher spatial frequencies as we approach the body. The classical representation of the gravity potential via the inverse powers of the radial variable is ill-suited for such an approach since its components do not decay fast enough. For this reason, estimation within that model is done typically all at once, fixing some degree of the approximation. Using a multiresolution approximation to the solution of Laplace's equation with a boundary value on the surface of a sphere, the individual terms have exponential decay allowing for a systematic estimation at different distances from the body. In addition to a multiresolution representation, we replace the spherical harmonics typically representing the angular part of the solution by the functions constructed using quadratures for the sphere invariant under the icosahedral group. Due to the low degree of the final gravity model estimated in this study, we do not use a localized version of these functions and, thus, only prove a concept that the spherical harmonics model can be replaced by functions with a much better localization. We foresee the use of a localized version of these functions for estimation the gravity field of primary bodies requiring high degree and order of the model (Ahrens and Beylkin, 2009), although further work is required in that direction.

Unlike the cubed-sphere gravity model, whose primary purpose is a fast evaluation of the gravity field (Beylkin and Cramer, 2002; Jones et al, 2010), the model of this paper is intended for estimation as it attempts to minimize the number of unknown parameters. We note that the radial part of this new model may be applied to the problem of fast evaluation as well. Once estimated, the model may be converted to the cubed-sphere model, but we do not address such a conversion for this study.

Interest in missions to small bodies, such as asteroids and comets, has grown considerably in recent years. One of the options proposed in the 2009 Review of the U. S. Human Spaceflight Plans Committee calls for the consideration of robotic and human missions to asteroids (Augustine et al, 2009). Beginning in 2000, the NEAR Shoemaker spacecraft (Cheng et al, 1997) inserted into orbit about the asteroid 433 Eros, and studied it for a year before landing. The Hayabusa satellite (Fujiwara et al, 2000) journeyed to 25143 Itokawa, and operated in a proximity of the asteroid for several months before landing, collecting a sample, and returning in June of 2010. Additionally, the DAWN satellite (Russell et al, 2004), which was launched in 2007, will explore the dwarf-planet Ceres and the asteroid 4 Vesta in the next three years. The ESA Rosetta (Glassmeier et al, 2007) mission, the joint Russia and China mission Phobos-Grunt (Marov et al, 2004), NASA/Goddard's proposed OSIRIS-REx, and the potential JAXA Hayabusa-2 are just a few of the planned missions to small bodies currently in development.

In this study, we do not address the issues of shape of the primary body and leave this issue for the future. We note that irregularly shaped bodies pose

problems for using the spherical harmonics models. As seen in Fig. 1 (generated from NEAR laser rangefinder results (Zuber et al, 2000)), the asteroid 433 Eros is roughly ellipsoidal in shape. For this reason, the ellipsoidal harmonics model is more appropriate than the spherical one. Results indeed demonstrate the advantages of the ellipsoidal harmonics gravity model (Garmier et al, 2002). For both the spherical and ellipsoidal harmonics models, the partial sum diverges for points within the circumscribing sphere (or ellipsoid), thus limiting the minimum valid altitude. Unfortunately, not all asteroids are ellipsoidal and, thus, other gravity representations suited for a more-or-less arbitrary shape are desired.
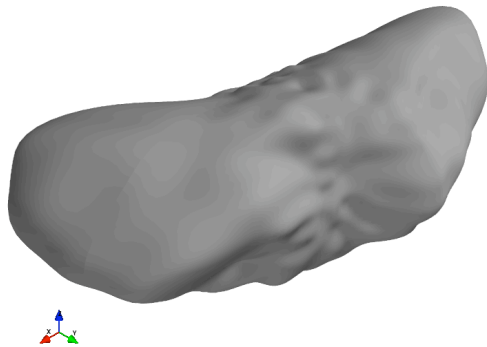
Fig. 1 An isometric view of the asteroid 433 Eros.

The goals of this paper are to introduce the new model and demonstrate its estimation capabilities. We accomplish this by applying the model to the asteroid 433 Eros, using the NEAR15A gravity model (Konopliv et al, 2002) derived from observations of the NEAR satellite. We start by presenting the MultiResolution representation and Quadratures for the Sphere (MRQSphere) model. This includes a description of the mathematical tools employed in defining the model, and their combination to create the model, and the specific choice of model parameters used in the paper. We then define the estimation method and present results from a simulation study. Finally, we provide conclusions and describe additional work required for its practical implementation.

2 MRQSphere Model

The MRQSphere model combines two recently developed mathematical tools to provide a multiresolution representation of the gravity field, i.e. a model with a resolution that varies with altitude. One of these tools approximates the radial decay of the gravity field using a sum of Gaussians, while the second one employs interpolation on the sphere to represent the angular variations. Using these tools, we evaluate a function on each one of a collection of spheres, or shells, and combine

the resulting values to determine the total gravity potential. In contrast to the inverse powers of the distance in the radial direction found in the standard spherical harmonic model, the approximation by Gaussians allows an efficient separation of regions with different spatial resolutions. Thus, the spatial resolution of the shells included in this model vary with altitude. Instead of using spherical harmonics to account for angular variations, we use a set of functions generated by a single function by centering it at quadrature nodes with a nearly even distribution over the sphere. These quadrature nodes are invariant under the icosahedral group and provide an analogue of Lagrangian interpolation on the sphere. The number of interpolation nodes varies with the degree of the function represented. We combine these tools to construct a multiresolution model of the gravity field.

In this section, we describe the mathematical tools employed to create the MRQSphere model. This includes a description of the quadratures for the sphere, and the approximation by Gaussians that allows for the multiresolution expression of the gravity field. We describe these tools, define the new model, and provide the equations for evaluating the gravity potential, acceleration, and variational equations. The final two sections describe the model configuration used to approximate the gravity field of the asteroid 433 Eros, and provide baseline results that characterize idealized performance of the model.

2.1 Quadratures for the Sphere

The standard model representing variations in the gravity field in the latitudinal and longitudinal directions uses the spherical harmonics, which are global functions on the sphere. An approach to replace them with better localized functions has been developed (Ahrens and Beylkin, 2009) and uses quadratures on the sphere invariant under the icosahedral group. Due to the invariance of the positions of the nodes under this discrete group, the nodes do not concentrate and have a near uniform distribution on the sphere. These quadratures are also near optimal, as far as the number of nodes required to integrate all spherical harmonics of a fixed degree and order. This combination of properties yields an analogue of the Lagrange-type interpolation on the sphere. As a result, we replace the spherical harmonics by a set of functions concentrated at the nodes of the quadrature and generated by a single function. Instead of estimating the coefficients of the spherical harmonics, the new quadratures allow direct estimation of the gravity field at the quadratures nodes. This section provides a brief introduction to the techniques introduced by Ahrens and Beylkin (2009).

The commonly used spherical harmonics model of the gravity potential may be expressed as

$$U(r, \phi, \lambda) = \frac{\mu}{r} \sum_{n=0}^{\infty} \left(\frac{R}{r}\right)^n \sum_{m=0}^{n} P_{n,m}[\sin \phi] \left(C_{n,m} \cos m\lambda + S_{n,m} \sin m\lambda\right). \quad (1)$$

After representing the radial distance in units of planetary radius $\rho \; (= r/R)$, we write

$$U(\rho, \phi, \lambda) = \frac{\mu}{R} \sum_{n=0}^{\infty} \rho^{-(n+1)} V_n(\phi, \lambda) \quad (2)$$

where

$$V_n(\phi, \lambda) = \sum_{m=0}^{n} P_{n,m}[\sin \phi] \left(C_{n,m} \cos m\lambda + S_{n,m} \sin m\lambda \right). \tag{3}$$

Instead of using the representation in Eq. 3, we want to represent V_n using its values on the sphere. For this purpose, we use the reproducing kernel (see Ahrens and Beylkin (2009)). Let $\mathcal{P}_N$ be the space of spherical harmonics of maximum degree and order N. The reproducing kernel

$$K_N(\boldsymbol{\alpha} \cdot \boldsymbol{\alpha}') \equiv \sum_{n=0}^{N} \frac{2n+1}{4\pi} P_{n,0}(\boldsymbol{\alpha} \cdot \boldsymbol{\alpha}'), \tag{4}$$

has the property that for any function f in $\mathcal{P}_N$, we have

$$f(\boldsymbol{\alpha}) = \int_{\mathbb{S}^2} K_N(\boldsymbol{\alpha} \cdot \boldsymbol{\alpha}') f(\boldsymbol{\alpha}') d\boldsymbol{\alpha}', \tag{5}$$

where $\boldsymbol{\alpha}$ and $\boldsymbol{\alpha}'$ denote unit vectors on the sphere $\mathbb{S}^2$. We note that $P_{n,0}$ is the Legendre polynomial and no associated Legendre functions are involved in the definition of K_N. If f is in $\mathcal{P}_N$, then it is unchanged by the operator in Eq. 5. If f resides in a wider subspace $\mathcal{P}_M$ where $M > N$, then the operator projects f onto $\mathcal{P}_N$. A detailed discussion of the kernel may be found in Ahrens and Beylkin (2009).

We next discretize Eq. 5 using quadratures with M nodes to integrate all functions in the subspace $\mathcal{P}_{2N}$ and obtain an analogue of Lagrange interpolation on the sphere. In Ahrens and Beylkin (2009), the location of the nodes ($\boldsymbol{\alpha}_i$) are chosen to be invariant under the rotations of the discrete icosahedral group, thus preventing them from concentrating at any particular location. As a result of discretization, we have

$$f(\boldsymbol{\alpha}) = \sum_{j=1}^{M} K_N(\boldsymbol{\alpha} \cdot \boldsymbol{\alpha}_j) w_j f(\boldsymbol{\alpha}_j) \tag{6}$$

where w_j are quadrature weights corresponding to the nodes $\boldsymbol{\alpha}_j$. The number of nodes M is chosen to integrate exactly the product of the two functions K_N and f, whose degree and order does not exceed $2N$. For example, for approximating the gravity field of degree 7, we use the number of nodes necessary to integrate the subspace $\mathcal{P}_{14}$. In Fig. 2, we provide examples where N refers to the maximum degree of the function in the Lagrange-type interpolation.

We illustrate the reproducing kernel K_N in Fig. 3. As the degree N increases, the function tends toward the delta function on the sphere. Thus, special care must be taken when evaluating Eq. 4 to prevent numerical error due to cancellation. Interpreting Eq. 4 as the Christoffel-Darboux formula (Szegö, 1975, Ch. 3), we obtain

$$K_N(\gamma) = \frac{N+1}{4\pi} \frac{P_{N,0}(\gamma) - P_{N+1,0}(\gamma)}{1 - \gamma}, \tag{7}$$

and using Szegö (1975, Eq. 4.5.4), we then arrive at

$$K_N(\gamma) = \frac{N+1}{4\pi} P_N^{(1,0)}(\gamma), \tag{8}$$

(a) 2N=14, 72 Points   (b) 2N=30, 372 Points
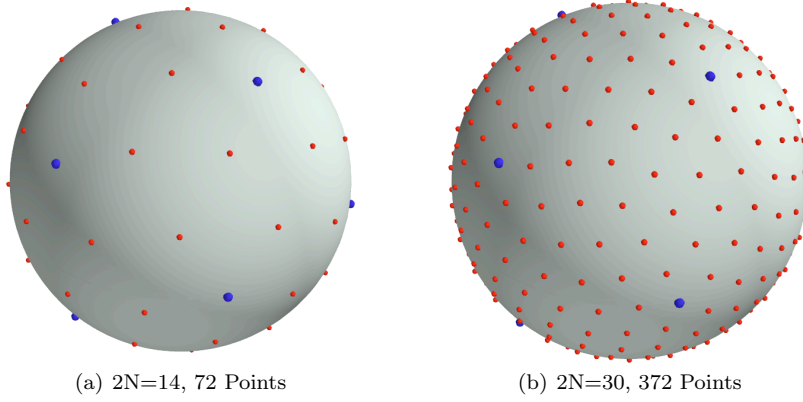
Fig. 2 Sample quadratures for the sphere for different degree models
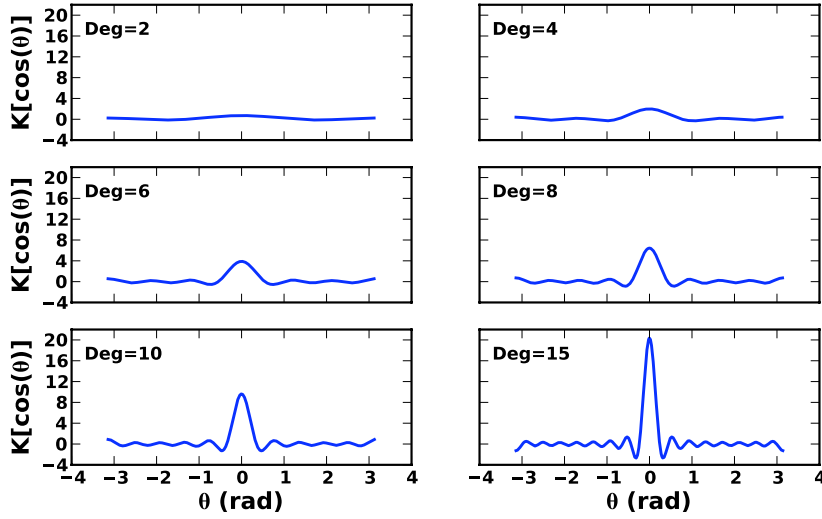
Fig. 3 Sample plots of the reproducing kernel K_N as a function of the angle between the vectors $\boldsymbol{\alpha}$ and $\boldsymbol{\alpha}'$ for various degrees N

where $P_N^{(1,0)}$ is the Jacobi polynomial with $\alpha=1$ and $\beta=0$. To simplify notation and prevent confusion of $P_N^{(1,0)}$ with the Legendre polynomials P_N, we denote

$$\bar{K}_N(\gamma) = P_N^{(1,0)}(\gamma) = \frac{4\pi}{N+1} K_N(\gamma). \tag{9}$$

and using the three term recurrence for Jacobi polynomials (Gradshteyn and Ryzhik, 2007, Eq. 8.961.2)), write

$$\bar{K}_n(\gamma) = (c_1\gamma + 1/c_0)\bar{K}_{n-1}(\gamma) - c_2\bar{K}_{n-2}(\gamma) \tag{10}$$

with

$$\bar{K}_0(\gamma) = 1 \tag{11}$$

$$\bar{K}_1(\gamma) = \frac{3}{2}\gamma + \frac{1}{2}. \tag{12}$$

and

$$c_0 = (n+1)(2n-1) \tag{13}$$

$$c_1 = (2n-1)(2n+1)/c_0 = (2n+1)/(n+1) \tag{14}$$

$$c_2 = (n-1)(2n+1)/c_0. \tag{15}$$

We use Equations 10 and 9 to compute values of the kernel $K_N(\gamma)$.

2.2 Approximation by Gaussians

To obtain a multiresolution representation instead of Eq. 2, following Beylkin and Monzón (2010), we replace $\rho^{-(n+1)}$ for all n by an approximation using Gaussians. Specifically, for any required precision $\epsilon > 0$, there exists a step size h and a positive M such that

$$\left| e^{-xy} - G_{h,M}(x,y) \right| \leq \epsilon \tag{16}$$

where

$$G_{h,M}(x,y) = \frac{hx}{\sqrt{4\pi}} \sum_{j=0}^{M} e^{-\frac{x^2}{4}e^{s_j} - y^2 e^{-s_j} + \frac{1}{2}s_j} \tag{17}$$

and

$$s_j = s_{start} + jh. \tag{18}$$

For details, we refer to Beylkin and Monzón (2010).

Since the $\rho^{-(n+1)}$ term in Eq. 2 may be rewritten as $e^{-(n+1)\ln\rho}$, applying Eq. 17 yields

$$\rho^{-(n+1)} \approx G_{h,\mathbb{Z}}(n+1, \ln\rho) = \frac{h(n+1)}{\sqrt{4\pi}} \sum_{j\in\mathbb{Z}} e^{-(n+1)^2 e^{-jh}/4 - (\ln\rho)^2 e^{jh} - jh/2}$$

$$= \frac{h(n+1)}{\sqrt{2\pi}} \sum_{j\in\mathbb{Z}} \sigma_j^{-1} e^{-(n+1)^2/(2\sigma_j^2)} e^{-(\ln\rho)^2\sigma_j^2/2} \tag{19}$$

where

$$\sigma^2 = 2e^{jh}. \tag{20}$$

Substituting Eq. 19 into Eq. 2 and reorganizing, we have

$$\tilde{U}(\rho,\phi,\theta) = \frac{\mu}{R} \sum_{j\in\mathbb{Z}} e^{-(\ln\rho)^2\sigma_j^2/2} Z_j(\phi,\theta) \tag{21}$$

where

$$Z_j(\phi, \theta) = \frac{h}{\sigma_j \sqrt{2\pi}} \sum_{n=0}^{\infty} (n+1) e^{-(n+1)^2/(2\sigma_j^2)} V_n(\phi, \theta). \qquad (22)$$

The sum in Eq. 21 extends over all integers $\mathbb{Z}$. However, most terms are negligible, and we designate a subset $\mathbb{J}$ of $\mathbb{Z}$ as the range of indices corresponding to the terms with significant contribution. We denote the truncated version of Eq. 21 as $\tilde{U}(\rho, \phi, \theta; \mathbb{J})$.
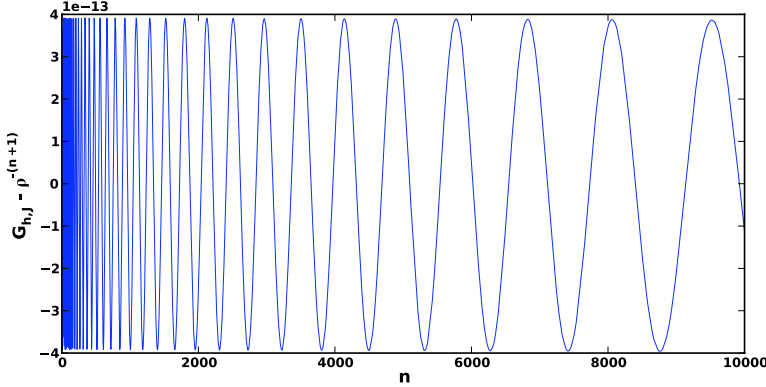
Fig. 4 Error in $G_{h,\infty}(\approx \rho^{-n})$ up to degree n for $\rho = 1 + \frac{0.25}{6378}$, $h=1/3$, and $\mathbb{J} = \{-30, \dots, 70\}$ (Beylkin and Monzón, 2010)

In Fig. 4, we provide the error for a sample set of parameters used with the function $G_{h,\mathbb{J}}$ described by Eq. 19. When generating $G_{h,\mathbb{J}}$, the specified accuracy ϵ determines the value h. The subset $\mathbb{J}$ is then found to meet these requirements for the given ρ. The error is uniform for all applicable n and will decrease for $\rho^n < 4 \times 10^{-13}$ with n sufficiently large.

2.3 Model

We now combine these mathematical tools to create the MRQSphere model of the gravity potential. Substituting the coordinates ϕ and λ with the unit vector $\boldsymbol{\alpha}$, we use $\tilde{U}(\rho, \boldsymbol{\alpha}; \mathbb{J})$, and represent the terms $Z_j(\boldsymbol{\alpha})$ in Eq. 22 using the analogue of Lagrange interpolation on the sphere, i.e. Equation 6. Thus, we write the MRQSphere model as

$$\tilde{U}(\rho, \boldsymbol{\alpha}; \mathbb{J}) = \frac{\mu}{R} \sum_{j \in \mathbb{J}} e^{-(\ln \rho)^2 \sigma_j^2/2} Z_j(\boldsymbol{\alpha}) \qquad (23)$$

$$Z_j(\boldsymbol{\alpha}) = \sum_{i=1}^{M} K_N(\boldsymbol{\alpha} \cdot \boldsymbol{\alpha}_i) w_i Z_j(\boldsymbol{\alpha}_i) \qquad (24)$$

In our approach we estimate functions $Z_j(\boldsymbol{\alpha})$ directly, thus avoiding any use of the spherical harmonics when evaluating the model. This Cartesian representation also eliminates any singularity at the poles when evaluating the acceleration. We note that, for a given accuracy, the exponential cutoff in Equation 22 allows us to predict the degree of the subspace of spherical harmonics for the functions Z_j and, thus, choose the appropriate number of quadrature nodes for estimation. We also note that, as described in Beylkin and Monzón (2010), the number of terms in Equation (21) depends only weakly on the required resolution and is relatively small. For a fixed ρ, only a few terms in Equation (21) contribute to the potential.

(a) Shell contributions (n=2) (b) Shell degree contribution
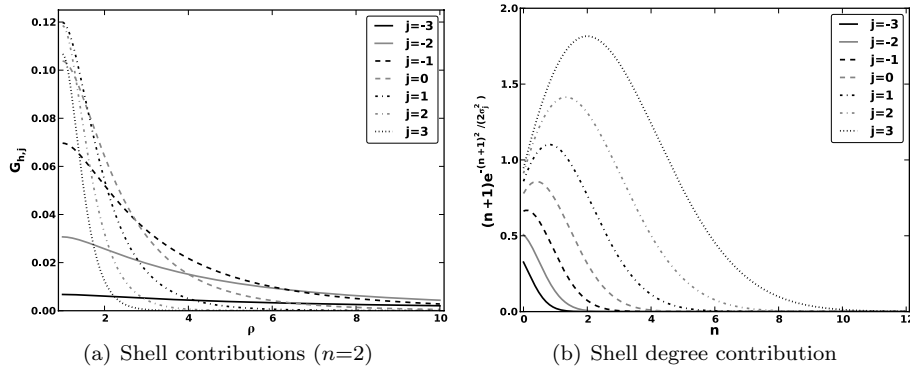
Fig. 5 The first figure illustrates the contributions of the different shells to the function $G_{h,\mathbb{J}}$ ($h = 0.5$) with variations in orbit radius (in units of R_E), while the second figure demonstrates the contribution of gravity degree n for a given shell

In Fig. 5, we plot the terms of the series in Eqs. 19 and 22 with $h = 0.5$. As seen in Fig. 5(a), points at low altitudes are highly dependent on the shells with a larger σ_j (corresponding to larger positive indices j). As altitude increases, these terms decay exponentially fast, and terms with smaller σ_j dominate the sum. For example, note in Fig. 5(a) the relative contribution of the $j = -2$ shell at ρ values of 1 versus 10. At $\rho = 10$, this shell provides the largest contribution to $G_{h,\mathbb{J}}$, but weakly affects the the value at low altitudes. Thus, only a small subset of shells are required when evaluating the gravity field at high altitudes, and the selection of shells depends on the user defined precision ϵ. As we may see in Fig. 5(b) a small σ_j implies a low degree n, and, conversely, a large σ_j value implies a larger degree. Thus, as expected, low-degree models are needed at high altitudes.

As derived in the Appendix A, for the acceleration vector we have

$$\ddot{\mathbf{r}} = \frac{\mu}{R} \sum_{j \in \mathbb{J}} e^{-(\ln \rho)^2 \sigma_j^2 / 2} \left[\left(-\frac{\sigma_j^2}{r^2} (\ln \rho) Z_j(\hat{\mathbf{r}}) \right) \mathbf{r} \right.$$

$$\left. + \left(\frac{\partial \hat{\mathbf{r}}}{\partial \mathbf{r}} \right) \left(\sum_{l=1}^{M} w_l Z_j(\boldsymbol{\alpha}_l) \frac{\partial K_n(\gamma)}{\partial \gamma} \boldsymbol{\alpha}_l \right) \right] \qquad (25)$$

Table 1 Configuration of the MRQSphere representation of the NEAR15A spherical harmonics model

Parameter	Value
Gaussian Stepsize (h)	0.425
Precision ϵ of approximating $\rho^{-(n+1)}$	5×10^{-10}
Relative accuracy of truncating the sum Z_j (Eq. 22)	7 significant digits

where we used matrix notation,

$$\frac{\partial \hat{\mathbf{r}}}{\partial \mathbf{r}} = \left(\frac{\partial \hat{\mathbf{r}}}{\partial \mathbf{r}}\right)^T = \frac{1}{r}\mathbb{I}_{3\times 3} - \frac{\mathbf{r}\mathbf{r}^T}{r^3}, \tag{26}$$

and $\mathbf{r}$ is the Cartesian position vector of the point of interest. We note that the outermost sum in Eq. 25 is now evaluated over the elements of $\mathbb{J}$ to match Eq. 23, i.e. to represent the acceleration determined by the MRQSphere model.

For variational equations, expressed in terms of derivatives (see Appendix A), we obtain

$$\frac{\partial^2 \tilde{U}}{\partial \mathbf{r}^2} = \frac{\mu}{R} \sum_{j \in \mathbb{J}} e^{-(\ln \rho)^2 \sigma_j^2/2} \left\{ \frac{Z_j(\hat{\mathbf{r}})\sigma_j^2}{r^2} \left(\frac{2\ln \rho + \sigma_j^2(\ln \rho)^2 - 1}{r^2}\mathbf{r}\mathbf{r}^T - (\ln \rho)\mathbb{I}_{3\times 3} \right) \right.$$
$$\left. - \left(\frac{2\sigma_j^2 \ln \rho}{r^2} \right) \mathbf{r} \left(\frac{\partial Z_j(\hat{r})}{\partial \mathbf{r}} \right)^T + \frac{\partial^2 Z_j(\hat{r})}{\partial \mathbf{r}^2} \right\}. \tag{27}$$

The sum of the diagonal of this matrix yields the Laplacian $\nabla^2 \tilde{U}$ of the model. Since $\tilde{U}$ is an approximation, $\nabla^2 \tilde{U} = 0$ for the MRQSphere model is not identically zero. However, since we control the precision the error can be made arbitrarily small. We compute the Laplacian for the MRQSphere model in Section 2.5 and show that the error is small and corresponds to the original choice of ϵ in the construction of the model.

2.4 MRQSphere Model for 433 Eros

We base the configuration of a model, i.e. the stepsize h and $\mathbb{J} \subset \mathbb{Z}$, on the model accuracy requirements dictated by the accuracy of measurements. For this paper, we focus on a model analogous to the low-degree, higher altitude model generated using radiometric and landmark data from the NEAR mission to 433 Eros. This 15x15 spherical harmonics gravity model (NEAR15A) (Konopliv et al, 2002) primarily used observations of the satellite at orbit radii of 2 Eros radii and above, where Eros radius $R_E = 16$ km. Only the gravity perturbations, i.e. gravity field terms of degree 2 or greater, are modeled by the MRQSphere model.

For the NEAR15A MRQSphere model, the selected parameters are provided in Table 1. Unlike the procedure used to generate Fig. 4, we begin with a specified h, ϵ, and $\mathbb{J}$, and determine the minimum ρ such that $|\rho^{-(n+1)} - G_{h,\mathbb{J}}(\rho)| < \epsilon$. Using this procedure, we generate Table 2. This table specifies the shells required when evaluating the MRQSphere model at a given altitude. For our MRQSphere model, 14 shells are required with indices $j = -5, \ldots, 8$ for orbit radii above 1.93 R_E. In this paper, we refer to a shell with index j as "shell j".

Table 2 Shells required at given radii (accurate to 10^{-5})

Range (in R_E)	$\mathbb{J}_{min}$	$\mathbb{J}_{max}$
Above 33.963085	-5	0
33.963085 - 17.221399	-5	1
17.221399 - 10.223156	-5	2
10.223156 - 6.437202	-5	3
6.437202 - 4.578281	-5	4
4.578281 - 3.412891	-5	5
3.412891 - 2.702480	-5	6
2.702480 - 2.244688	-5	7
2.244688 - 1.925941	-5	8
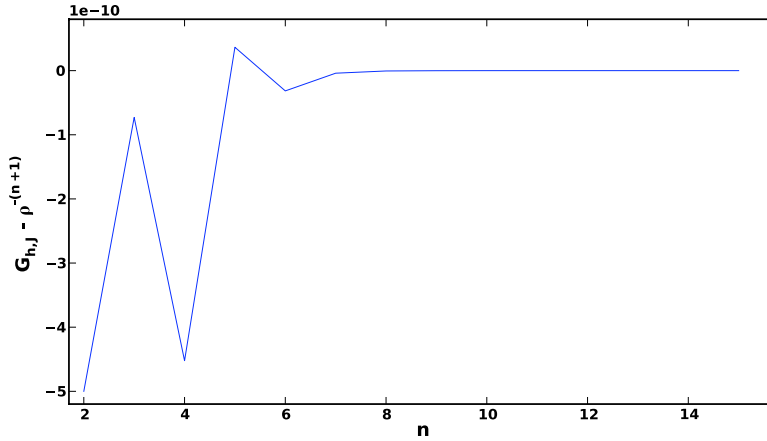
Fig. 6 Precision (in units of 10^{-10}) of the approximation by Gaussians of $\rho^{-(n+1)}$ using shells -5 through 1 at a radius of 17.2214 R_E

In Fig. 6 we illustrate the precision of approximating $\rho^{-(n+1)}$ using Gaussians with the parameters shown in Table 1. We see in this figure that, unlike at the other altitude ranges listed in Table 2, the corresponding shells at slightly above the radius 17.221399 barely meet the precision requirement of 5×10^{-10}. This influences future results, specifically, the precision of the MRQSphere model as the radius of decreases towards 17.22 R_E. The upper boundary for including shell 2 may be changed to avoid this phenomenon but we have not done so intentionally

With the subset $\mathbb{J}$ now specified, the shell degrees, and thus the number of quadrature nodes required, may be determined. We select the number of terms in Z_j to achieve a relative accuracy of 7 significant digits and provide the resulting values in Table 3. Quadratures on the sphere are currently available only for particular degrees, thus for a given j we use the minimal number of nodes that guarantees proper integration. We denote the corresponding degree as n_{max}. Additionally, we place a limit of degree 15 on the shells given that the NEAR15A model is 15×15.

Table 3 Required gravity field degree (n_{max}) and the number of quadrature nodes for each shell

$j \in \mathbb{J}$	n_{max}	M	$j \in \mathbb{J}$	n_{max}	M
-5	4	32	2	14	312
-4	4	32	3	15	372
-3	4	32	4	15	372
-2	7	72	5	15	372
-1	7	72	6	15	372
0	9	132	7	15	372
1	11	192	8	15	372

2.5 Baseline Performance

To provide a basis of comparison, and gain a more thorough understanding of the ideal performance of the MRQSphere model used for this study, we perform a set of baseline tests. The results of these tests profile the accuracy of the model given the true NEAR15A spherical harmonics model, which we used to estimate the functions Z_j at the quadrature nodes.

We define the number of common digits

$$CD = \log_{10} \left| \frac{a_{SH}}{a_{QS} - a_{SH}} \right|, \tag{28}$$

where QS and SH refer to the MRQSphere and spherical harmonics models, respectively. In the case of acceleration, we treat each component of the vector separately.
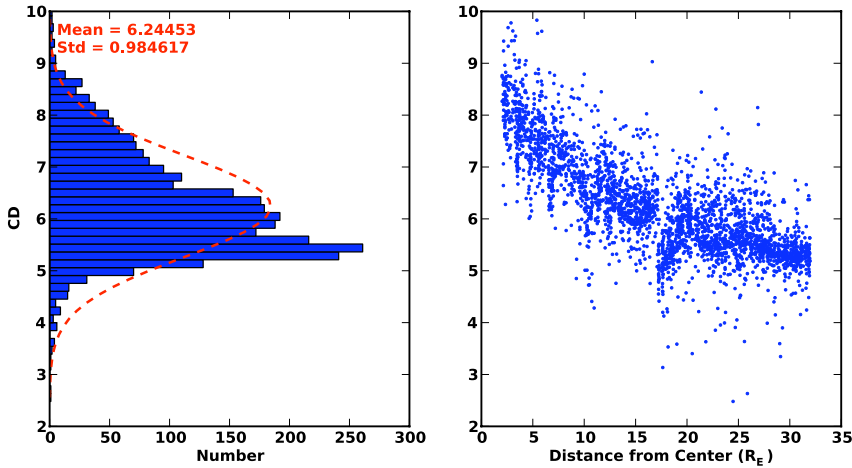
Fig. 7 Precision of the nominal MRQSphere model with the spherical harmonics model, defined by the number of common digits between them, with the figure on the right illustrating the distribution of accuracy with radius

A comparison of the MRQSphere model accelerations with those of the spherical harmonics model is provided in Fig. 7. As the radius decreases, the precision improves. For a fixed ϵ, which controls the approximation via Gaussians, the number of accurate digits in Eq. 19 increases for lower altitudes. As the radius decreases towards 17 R_E, the precision deteriorates slightly. We associate this deterioration with slightly reduced accuracy at this radius as described in Fig. 6.
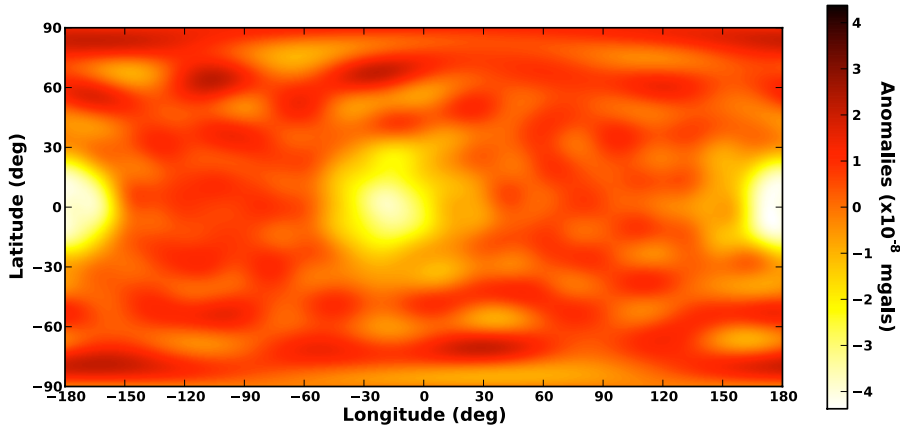
Fig. 8 Precision of the nominal MRQSphere model and the spherical harmonics at $2R_E$

In Fig. 8, we illustrate the spatial distribution of gravity anomalies, when compared to the spherical harmonics model. The regions with the largest anomalies correspond to the locations of the extremal locations of the asteroid, and correspond to the largest gravity variations as determined by the spherical harmonics model (Konopliv et al, 2002).

To demonstrate the Laplacian of the MRQSphere model is close to zero, we provide experimental evidence that demonstrates that the error corresponds to the selected accuracy of the model. The Laplacian is evaluated via Eq. 27 by adding the diagonal elements of the resulting 3×3 matrix. We calculate the relative error between the resulting sum and the largest value on the diagonal. A histogram of the numerically computed values are included in Fig. 9, which demonstrates the Laplacian error is approximately 10^{-5}, with a worst-case error of 10^{-3}. Similar to the accuracy of the acceleration vector, the error for the Laplacian of the model becomes smaller as altitude decreases. However, these results demonstrate increased variations in the model accuracy near the shell boundaries. This is apparent for the higher altitudes tested in Fig. 9 where the altitude range is larger.

Figure 10 demonstrates that, like the acceleration vector, the Laplacian has a spatial dependence. Specifically, the regions near the side lobes of the asteroid, where gravity variations are greatest, exhibit a reduction in accuracy.

To characterize the effects of this model's accuracy on orbit propagation, we numerically integrate an initial satellite state forward in time for 24 hours using the MRQSphere model. We then compare the results to trajectories generated via
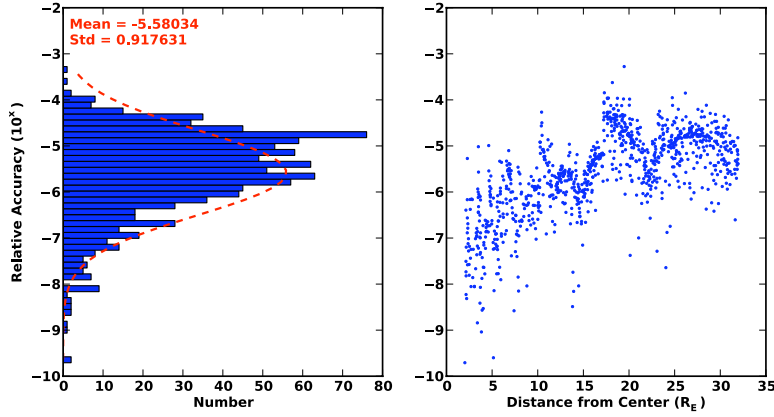
Fig. 9 Relative accuracy of the Laplacian ($\nabla^2 \tilde{U}$) of the idealized MRQSphere model when compared to the maximum diagonal element of the variational equation matrix, with the figure on the right illustrating the distribution of significant digits with radius
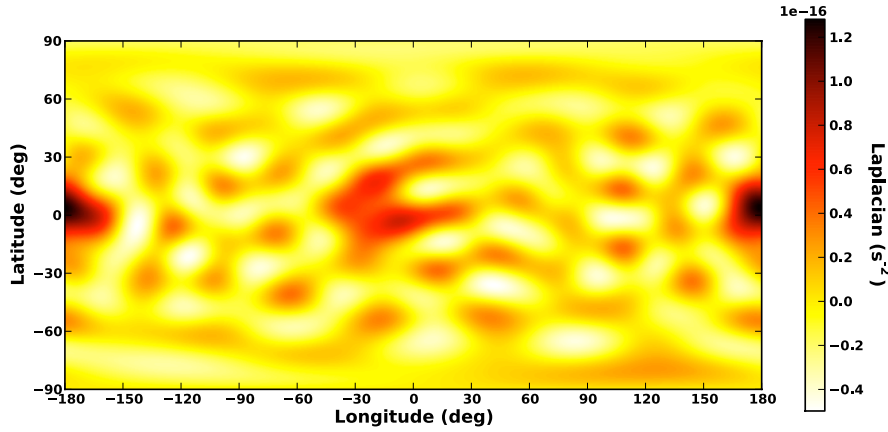
Fig. 10 Laplacian for the nominal h=0.425 MRQSphere model at $r = 2R_E$

the spherical harmonic model. We consider orbits at an altitude of 17 km, i.e. the minimum valid radius of our generated model, and from 20 to 150 km in increments of 5 km. At each altitude, we propagate approximately 1,300 state vectors uniformly spaced in inclination and right ascension of the ascending node. Each orbit is initially circular, with all other orbit elements set to zero. For integration, we use the Runge-Kutta 7(8) algorithm described by Fehlberg (1968) with an integration tolerance of 10^{-12}.

In Figure 11, we present the orbit propagation accuracies of the MRQSphere model. Differences are relative to orbits propagated with the NEAR15A spherical
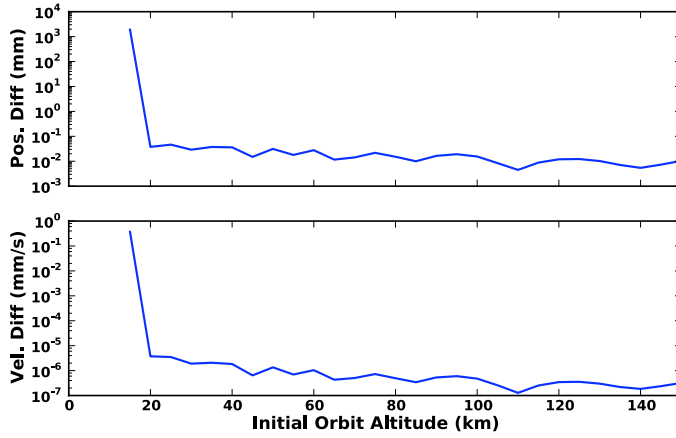
Fig. 11 Summary of 3D RMS orbit propagation errors using the baseline MRQSphere model for Eros.
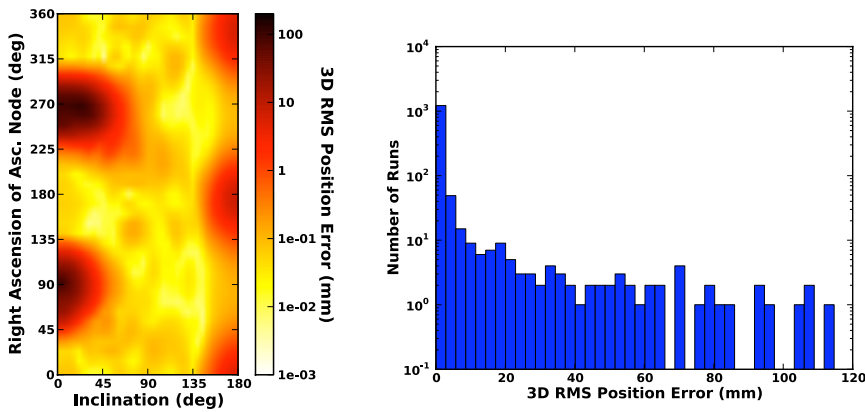
Fig. 12 Distribution of 3D RMS differences for propagated orbits initially at 17 km with the nominal Eros MRQSphere model.

harmonic model, and computed over all orbits at all times. Results demonstrate a maximum 3D RMS orbit propagation accuracy at a fraction of a millimeter, except for orbits initially at 17 km in altitude.

In Figure 12, we provide detailed results for the 17 km orbits. We note that the y-axis of the histogram is logarithmic. As indicated by the contour plot, equatorial orbits result in the largest error. Further investigation demonstrates that interactions with the lobes of Eros cause a decrease in altitude to a region below the valid altitude range of this MRQSphere model.
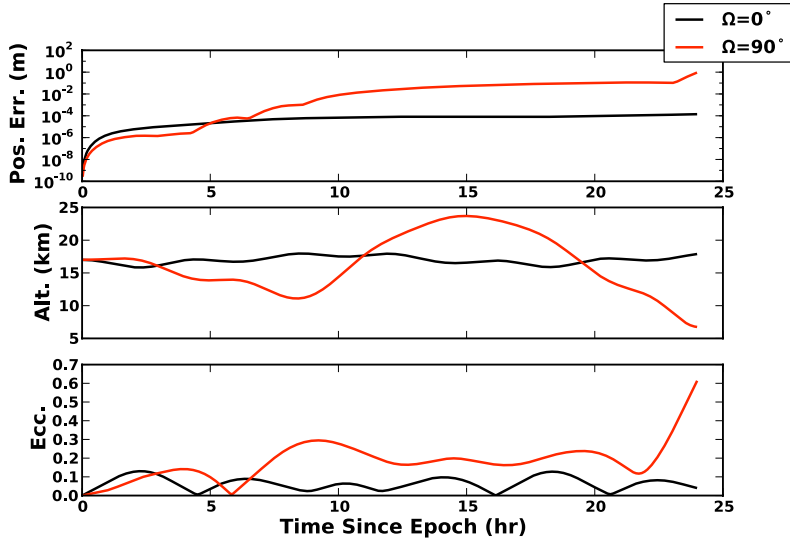
Fig. 13 Orbit propagation properties for two equatorial orbits about 433 Eros.
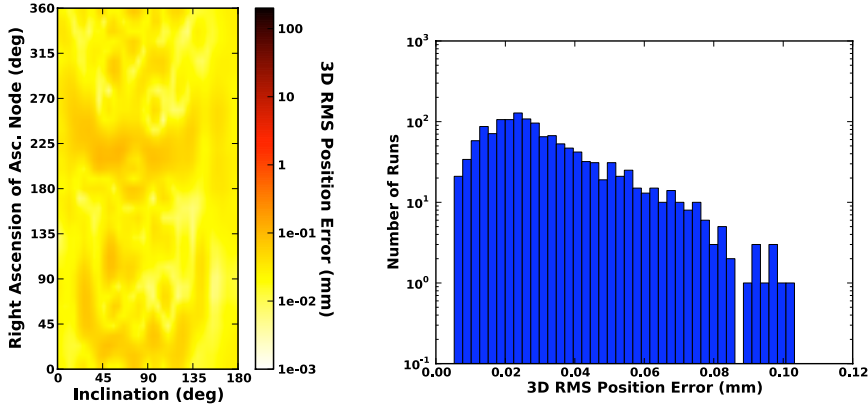
Fig. 14 Distribution of 3D RMS differences for propagated orbits initially at 20 km with the nominal Eros MRQSphere model.

For Figure 13, we propagated two equatorial orbits, one each initially at Ω values of $0°$ and $90°$. The figure illustrates the propagation error and the simulated orbit altitude and eccentricity. Due to the relatively fast rotation rate of Eros, orbits initially at right ascensions close to $90°$ and $270°$ have extended periods of interactions with the lobes. These interactions exert a larger torque on the orbit, thus changing the orbit elements. In this case, it forces the radius of periapsis to drop below $2 R_E$, and, hence, below the minimum orbit altitude for this MRQ-

Sphere model. We note that equatorial orbits within approximately 2 R_E in radius correspond to the regions of instability derived in Scheeres (2002).

For the purpose of comparison, we provide details on the orbits initially at an altitude of 20 km in Figure 14. These orbits remain within the range covered by the MRQSphere model, and, thus, errors are less than 0.11 mm.

3 Model Estimation

In this section, we describe the estimation procedure used in this study. First, we describe the estimated state and the observations used, followed by a description of the estimation algorithm employed. Additionally, we define a redistribution technique that allows us to correctly distribute the estimated gravity field among the shells. Finally, we provide and discuss results of the estimation process.

3.1 Least-Squares Estimation Using SVD

Assume the vector $\mathbf{x}$ is comprised of n unknown elements. Let $\mathbf{y}$ be a vector of m observations, which are related to the estimated state vector by the $m \times n$ $(m > n)$ matrix H, and

$$\mathbf{y} = H\mathbf{x} + \boldsymbol{\nu}. \tag{29}$$

where $\boldsymbol{\nu}$ denotes the modeling or observations errors. The ordinary least-squares algorithm seeks a vector $\hat{x}$ that minimize the sum of the squares of these residuals. Assuming H is of rank n and $E[\boldsymbol{\nu}\boldsymbol{\nu}^T] = I_{m \times m}$, the normal form of the solution to the least squares algorithm (Tapley et al, 2004) is

$$\hat{x} = \left(H^T H\right)^{-1} H^T \mathbf{y}. \tag{30}$$

We note that the product $H^T H$ squares the condition number of the observation mapping matrix, potentially reducing the number of recoverable significant digits when using fixed precision floating-point arithmetic.

If the observations are not weighted equally, i.e. $E[\boldsymbol{\nu}\boldsymbol{\nu}^T] = B$ where B is diagonal but not the identity matrix, then a scale factor is required. Thus, premultiplying both sides of Eq. 29 by $\sqrt{B^{-1}}$, yields the weighted least squares solver

$$\hat{x} = \left(H^T B^{-1} H\right)^{-1} H^T B^{-1} \mathbf{y}, \tag{31}$$

where the square-root of a nonnegative matrix is defined in the usual manner.

If the rank of H is less than n, or the condition number is sufficiently large, then Eqs. 30 and 31 may not provide an adequate solution. In these cases, we use the singular value decomposition (SVD), writing

$$H = WSV^T \tag{32}$$

where both W and U are unitary matrices (i.e. $V^T V = I$), and S is a diagonal matrix with singular values. Explicitly indicating zero singular values, we write

$$S = \begin{bmatrix} S' & 0 \\ 0 & 0 \end{bmatrix} \tag{33}$$

where the $r \times r$ matrix S' contains the non-zero singular values and r is the numeric rank of H. We assume that singular values below a certain threshold are set equal to zero. The pseudoinverse of H is calculated using SVD, and solutions of Eq. 29 may be expressed as

$$\hat{x} = V \begin{bmatrix} S'^{-1} & 0 \\ 0 & 0 \end{bmatrix} W^T \mathbf{y}. \tag{34}$$

For the weighted least squares using SVD, the solution is written as

$$\hat{x} = V \begin{bmatrix} S'^{-1} & 0 \\ 0 & 0 \end{bmatrix} W^T \sqrt{B^{-1}} \mathbf{y}, \tag{35}$$

where

$$\sqrt{B^{-1}} H = V^T S W. \tag{36}$$

The state-error covariance matrix, $E[(\hat{x}-\mathbf{x})(\hat{x}-\mathbf{x})^T]$, where $\mathbf{x}$ is the true state, provides some statistical information on the quality of the solution $\hat{x}$. In the case of the least-squares algorithm with SVD, it may be shown that (e.g., see Ahn, 1996)

$$E[(\hat{x} - \mathbf{x})(\hat{x} - \mathbf{x})^T] = V \begin{bmatrix} S'^{-2} & 0 \\ 0 & 0 \end{bmatrix} V^T. \tag{37}$$

3.2 Estimation Process

Missions to bodies beyond Earth orbit often utilize a statistical filter, usually a square-root information filter (SRIF), to estimate the satellite position, gravity field, and other parameters using radio science and other observations available. To simplify the gravity recovery process for this proof of concept, we only estimate the terms of the gravity field. We assume the satellite state is known, with measurements of the gravity potential provided with some accuracy. Furthermore, we only estimate the Z_j values for a single shell at a time as we approach the asteroid. Thus, our estimated state vector is

$$\mathbf{X}_j = \begin{bmatrix} \sqrt{w_1} Z_j(\boldsymbol{\alpha}_1) \\ \sqrt{w_2} Z_j(\boldsymbol{\alpha}_2) \\ \vdots \\ \sqrt{w_M} Z_j(\boldsymbol{\alpha}_M) \end{bmatrix} \tag{38}$$

where M is the number of nodes for a given shell. The reason for the $\sqrt{w_j}$ factor will be explained below, but we then rewrite Eq. 6, in terms of Z_j, as

$$Z_j(\boldsymbol{\alpha}) = \sum_{i=1}^{M} K_N(\boldsymbol{\alpha} \cdot \boldsymbol{\alpha}_i) \sqrt{w_i}(\sqrt{w_i} Z_j(\boldsymbol{\alpha}_i)). \tag{39}$$

Additionally, we constrain the observations to include those of the satellite within the altitude range for a single MRQSphere shell, and only one shell is estimated at a time. We first estimate the outermost shell, and then reduce the altitude range to estimate the next shell (given estimates of all previous shells). Since the

MRQSphere model starts with the initial range of shells -5 through -1, we must assume an a priori estimate of these shells is available. Section 3.4 discusses how this may be accomplished.

Since we only estimate one shell at a time, designated as shell j, contributions of previously estimated shells to the observed potential must be removed. Our observation U_i' is thus

$$U_i' = \frac{R_E}{\mu} \left(U_i - \frac{\mu}{|\mathbf{r}_i|} - \sum_{k=j_{min},\ldots,j-1} \tilde{U}(\mathbf{r}_i; \mathbb{J} = \{k\}) \right) \tag{40}$$

where U_i is the original observation and j_{min} is the lowest index in the MRQSphere model. Note that we have also removed the two-body contribution and scaled the observation by μ/R_E to simplify the computations. This also makes the value of U_i' dimensionless with a typical magnitude on the order of 10^{-8}. We add Gaussian noise to the observation with zero mean and a standard deviation of 1×10^{-11}. This noise was selected to provide 3-5 digits of accuracy in the observation, which matches the corresponding parameters selected for the MRQSphere model. The resulting state to observation mapping matrix H for observation U_i' at $\mathbf{X}_i$ is

$$H = \left[e^{-\left(\ln \frac{|\mathbf{r}_i|}{R_E} \right)^2 \sigma_j^2/2} K_N(\hat{r}_i \cdot \boldsymbol{\alpha}_1) \sqrt{w_1} \ldots e^{-\left(\ln \frac{|\mathbf{r}_i|}{R_E} \right)^2 \sigma_j^2/2} K_N(\hat{r}_i \cdot \boldsymbol{\alpha}_M) \sqrt{w_M} \right]. \tag{41}$$

In Fig. 15, we provide the singular values of the H matrix defined in Eq. 41 when estimating the $j{=}0$ shell. As illustrated, H is not full rank and the ordinary least-squares algorithm will not suffice. Thus, we use the SVD algorithm for estimating the MRQSphere gravity field with scaled singular values less than 10^{-15} set to zero.
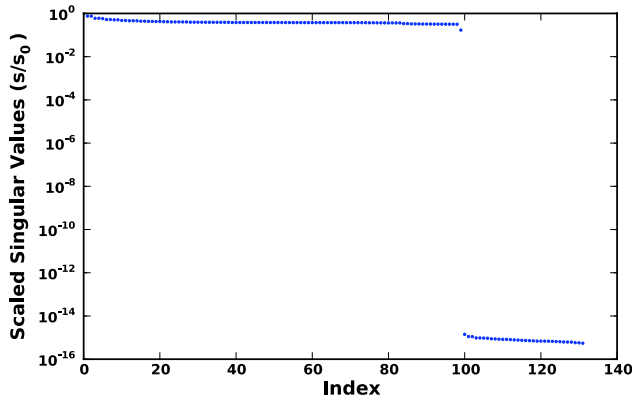
Fig. 15 Singular values for the H matrix when estimating the $j{=}0$ shell with 132 nodes

To model the observations, we simulate a collection of satellite orbits using the full NEAR15A spherical harmonics gravity model, which we consider the true

gravity field. We note that these trajectories are independent of those used in the orbit propagation tests of Section 2.5. Using the NEAR15A model, we evaluate the potential at points on these orbits to generate the observations U_i. Nine sets of observations are generated, one each for the range of orbit radii in Table 2. Thus we have one set of observations for each of the shells indexed from 0 through 8. We propagate orbits long enough to provide (roughly) complete coverage of the gravity field, i.e. groundtracks overlay the full surface of the asteroid, and sample the orbit in 5 minute increments. The initial sidereal time of the asteroid was $0°$ with a rotation rate of 3.3116598×10^{-4} rad/s.

3.3 Estimated Gravity Field Redistribution

Since the shells, as defined by Gaussians, overlap, the estimation process does not control how a contribution of a particular degree n influences the model. Thus, estimated functions Z_j may deviate from their definition in Eq. 22. To match the estimated function Z_j to that definition, we use projectors onto the subspace of the spherical harmonics.

As mentioned in Section 2.1, the reproducing kernel in Eq. 5 is essentially a projector. However, we now wish to create the discretized form of this projection operator using the quadrature nodes. Let us consider a function f in the subspace $\mathcal{P}_n$ and the kernel K_m, where $m \le n$. By multiplying both sides of Eq. 6 by $\sqrt{w_i}$, we have

$$\sqrt{w_i} f_m(\boldsymbol{\alpha}_i) = \sum_{j=1}^{M} (\sqrt{w_i} K_m(\boldsymbol{\alpha}_i \cdot \boldsymbol{\alpha}_j) \sqrt{w_j})(\sqrt{w_j} f_n(\boldsymbol{\alpha}_j)), \qquad (42)$$

where the number of nodes M is sufficient to discretize Eq. 6 exactly. The matrix $\mathcal{K}_m$, with elements $\sqrt{w_i} K_m(\boldsymbol{\alpha}_i \cdot \boldsymbol{\alpha}_j) \sqrt{w_j}$, is a projector on the subspace $\mathcal{P}_m$ from the subspace $\mathcal{P}_n$. In other words, this projector provides a means for generating values at the nodes of the lower degree function f_m using values at the same nodes of the higher-degree function f_n. We note that the eigenvalues of the $\mathcal{K}_m$ matrix are either 1 or 0. The inclusion of $\sqrt{w_j}$ in Eq. 42 is the reason we used these factors in Eq. 38.

We now describe a method for using these projectors to properly distribute the gravity field among the shells of the MRQSphere model. First, we select a shell with index j and associated quadrature nodes at $\boldsymbol{\alpha}_k$ (usually the last shell estimated), which models the function Z_j of degree n. Next, we evaluate the currently estimated potential $\tilde{U}(\rho \boldsymbol{\alpha}_k; \mathbb{J} = \{j_{min}, \dots, j\})$ at the nodes of the selected shell j. In this case, ρ is the lowest valid radius for the model using only shells j_{min} through j. Applying the projector, we generate the values $\sqrt{w_i} U_m(\boldsymbol{\alpha}_i)$ at each of the quadrature nodes, where $U_m(\boldsymbol{\alpha}_i)$ refers to the potential of degree m. We perform this operation for each degree $m = 2, \dots, N-1$. Rearranging Eq. 2 and multiplying by $\sqrt{w_i}$, we have

$$\sqrt{w_i} V_m(\boldsymbol{\alpha}_i) = \left((\sqrt{w_i} U_m(\boldsymbol{\alpha}_i)) - \sum_{p=2}^{m-1} \rho^{-(p+1)} (\sqrt{w_i} V_p(\boldsymbol{\alpha}_i)) \right) \rho^{m+1}$$

$$= ((\sqrt{w_i} U_m(\boldsymbol{\alpha}_i)) - (\sqrt{w_i} U_{m-1}(\boldsymbol{\alpha}_i))) \rho^{m+1}. \qquad (43)$$

Thus, after mapping the full estimated gravity potential to the lower degree subspaces, we now have a representation of $V_m(\boldsymbol{\alpha}_i)$ for $m = 2, \ldots, N - 1$. Using

$$V_m(\beta_k) = \sum_{i=1}^{M} K_m(\beta_k \cdot \boldsymbol{\alpha}_i) \sqrt{w_i}(\sqrt{w_i} V_n(\boldsymbol{\alpha}_i)), \qquad (44)$$

we compute the mth degree projections at the nodes β_k of any lower-index shell in the MRQSphere model. Finally, we combine Eqs. 44, 21, and 22 to recompute values at the nodes for all shells. Through this process, the information on the gravity field is properly distributed among the shells of the MRQSphere model.
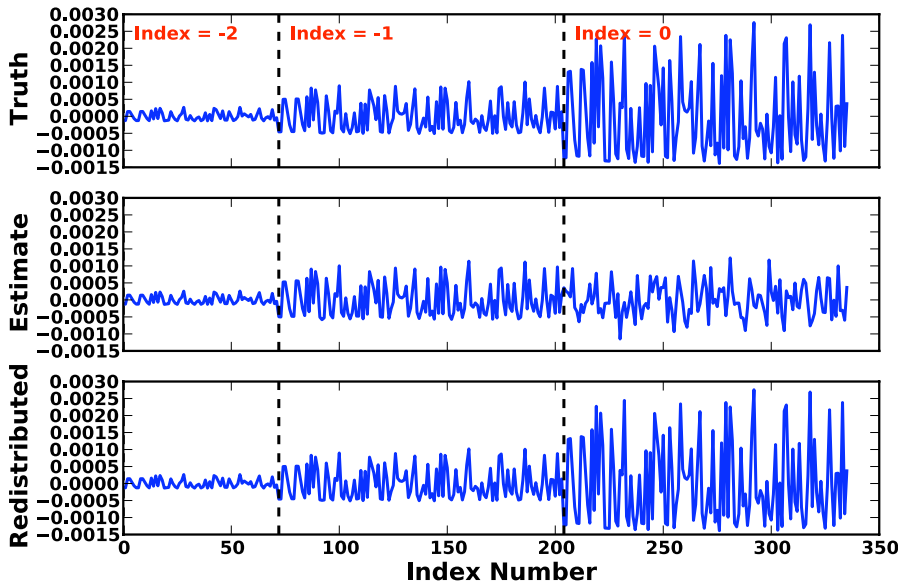
Fig. 16 Example improvement in gravity field estimation when using the redistribution algorithm with the MRQSphere model

In Fig. 16, we illustrate the effect of this redistribution process. For this example, we use the SVD algorithm to simultaneously estimate shells -2, -1, and 0. The SVD least-squares algorithm appears to estimate shells -2 and -1 correctly, but not shell 0. However, the overall fit to the data is within the measurement noise. After applying this redistribution algorithm, we recover the correct values on the shell 0. Although it is not apparent in the pictures, the accuracy of shells -2 and -1 is also slightly improved.

We note that the current redistribution algorithm does not include a correction of the state-error covariance matrix. Solving this issue has been designated as future work.

Table 4 MRQSphere determined acceleration precision (mean CD and standard deviation) with the true spherical harmonics model for various combinations of a priori estimates and state vectors

Shells Estimated (j index)	Zeros	Low Accuracy	True
-5, -4, -3, -2, -1, 0	3.511/.698	3.399/.698	3.340/.769
-2, -1, 0	2.866/.726	2.789/.730	3.288/.760
0	4.073/.668	5.416/.727	5.394/.695

3.4 Estimation Results

As mentioned previously, we assume a low-degree spherical harmonics model is available to initialize shells -5 through -1 in the MRQSphere model. Let us show that a low-accuracy, low-degree spherical harmonics model valid at large distances is sufficient to satisfy this assumption. For this purpose, we conduct three groups of tests. First, we assume no a priori knowledge of the gravity field. Second, we assume that a low-accuracy spherical harmonic model, valid at large distances, is available. Finally, we assume a full, true spherical harmonic gravity model for comparison. We calculate the initial estimates of shells -5 through -1 using this a priori gravity model. We also consider the outcome as a function of which shells participate in estimation.

To generate the low-accuracy spherical harmonic model, we scale the 1-σ standard deviations for each term of the NEAR15A model by 10,000. We selected this value to yield a σ for the $C_{2,0}$ term on the same order of magnitude as $C_{2,0}$. We then apply Gaussian noise with zero mean and the scaled σ to the true value. For the zonal terms through degree 4, this generates a Stokes coefficient on the same order of magnitude as its true value. For all other terms, the σ value may be orders of magnitude greater than the NEAR15A coefficient. We expect that, in practice, initial estimates of the gravity field will be more accurate than that. Before spacecraft rendezvous, an initial estimate of the gravity field may be generated using radar imaging of the asteroid. In this case, evaluation of surface integrals over the resulting polyhedron shape of the small body yields a low-degree spherical harmonics model. Tsoulis et al (2009) describes how to generate such a model. Additionally, an initial low-degree spherical harmonics model may be generated using a series of asteroid flybys before capture (Takahashi and Scheeres, 2010).

Table 4 presents the statistical accuracy of the resulting acceleration vectors for the different a priori models after estimating all shells. The table also illustrates the effects of increasing the number of shells estimated using the first data set. Shells one through eight are estimated individually for all tests. We note that there is no statistical difference in estimating only shell zero with either a low accuracy a priori gravity model or a true gravity model. However, the effects of providing no initial gravity model has a noticeable impact. For the remainder of this section, we examine results for the estimation of shell 0 with the low-accuracy gravity model.

In Fig. 17, we provide a histogram of the precision of the acceleration vectors with those determined by the spherical harmonics model. Unlike the baseline results presented in Fig. 7, precision is roughly uniform for all radii. For the baseline model, ϵ determine the absolute limit of the MRQSphere model accuracy. As expected, the estimation problem further limits accuracy based on the estimation algorithm employed and the measurement accuracy. In this case, measurement ac-
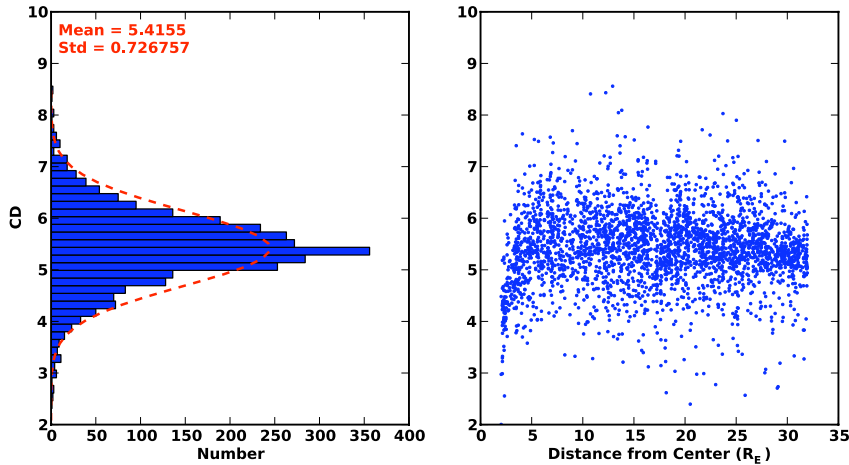
Fig. 17 Precision of the estimated MRQSphere model with the spherical harmonics model, defined by the number of common digits between them, with the figure on the right illustrating the distribution of accuracy with radius

curacy of 4 or 5 digits yields a model accurate to just as many digits. The decrease in precision for low altitude points, i.e. points requiring the evaluation of shell 8, is a result of reduced accuracy for the final shell estimated. If the estimation process had been truncated with shell five and only points above 4.6 R_E were tested, results demonstrate this downward trend would still be seen. These results have not been provided in the interest of brevity.

Figure 18 provides the relative accuracy of the Laplacian of the estimated model. Unlike the acceleration vector, there is a small radial dependency on the accuracy of the Laplacian, especially as the radius decreases towards 17.22 R_E. Like the idealized model results of Fig. 9, the ability of the Laplacian to satisfy the constraints of potential theory depends on the accuracy of the model. In this case, an MRQSphere accurate to 5 digits yields a Laplacian with a relative accuracy of approximately 10^{-5}.

Figure 19 illustrates the spatial distribution of errors in the estimated MRQSphere model. Errors do not correspond to regions of high gravity variability, but are more coupled with the distribution of measurements over the surface of the asteroid. In Fig. 20, we process observations for shell 8 with large regions deprived of measurements. Peak anomalies on the plot correspond to regions with no observations and have doubled in magnitude. Regions with observations exhibit results mostly comparable to those in Fig. 19. Of course, this is an issue with spherical harmonics gravity model as well. A primary example of this phenomenon is estimation of the lunar gravity field where little is known about the Moon's far side gravity terms (Konopliv et al, 2001).

In Figure 21, we provide the degree variances of the NEAR15A model, the nominal and estimated MRQSphere models, the differences between the MRQSphere models and the NEAR15A, and the estimated error in the NEAR15A model. To generate the variances for the nominal MRQSphere model, we evaluate the poten-
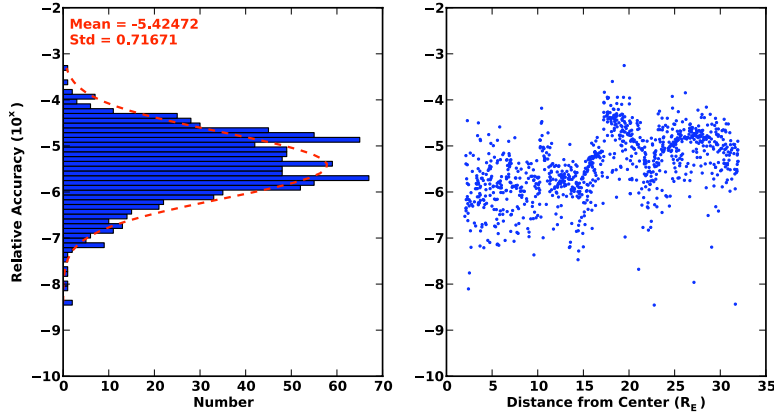
Fig. 18 Relative accuracy of the Laplacian ($\nabla^2\tilde{U}$) of the estimated MRQSphere model when compared to the maximum diagonal element of the variational equation matrix, with the figure on the right illustrates the distribution of significant digits with radius
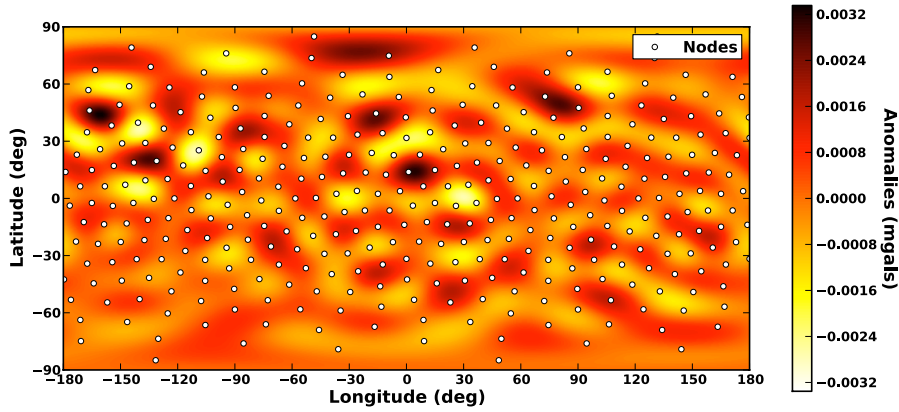
Fig. 19 Gravity anomalies for estimated h=0.425 MRQSphere model at R=$2R_E$

tial at 2,000 random points with a radial distance of 2 R_E. Given the resulting values of potential, we perform a least squares fit to generate the spherical harmonic model, specifically the $C_{n,m}$ and $S_{n,m}$ coefficients in Eq. 3, that represents this nominal model. We then compute the sum of the squares for all coefficients of a given degree n, and repeat this procedure for the estimated MRQSphere model. This figure indicates that the MRQSphere closely approximates the degree variances of the defined truth model up to degree 14. As stated in Konopliv et al (2001) and seen in Figure 21, the NEAR15A model reasonably approximates the Eros gravity field to degree 10. Although the MRQSphere model closely approxi-
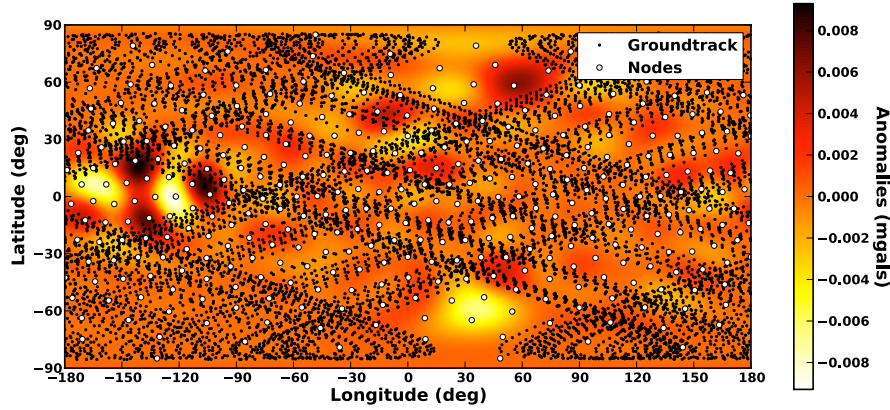
Fig. 20 Gravity anomalies for estimated h=0.425 MRQSphere model at R=$2R_E$ with spatial gaps in data
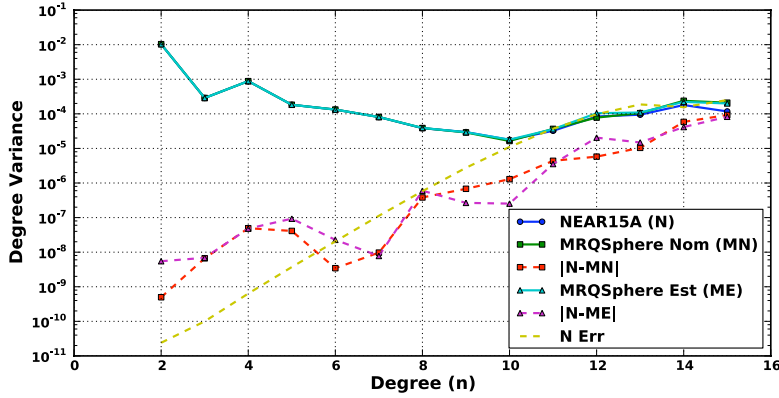
Fig. 21 Degree variances for the nominal and estimated MRQSphere models, the NEAR15A model, and their errors

mates the truth to degree 14, this is possibly an optimistic assessment of its gravity estimation capabilities given the simplification of this proof-of-concept study.

Figure 22 illustrates the 3D RMS orbit propagation error after 24 hours using the same method as that of the orbit propagation test in Section 2.5. In this discussion, we ignore orbits at altitudes less than 1 R_E since such orbits correspond to regions of orbit instability, and propagation errors are also a product of orbit altitudes below the applicable range of the MRQSphere model. Orbits initially at a 20 km altitude, corresponding to the range required for shell eight, have a 3D RMS accuracy on the order of 1 m. This error decreases with altitude as the absolute error of the estimated MRQSphere model decreases, i.e. the two-body
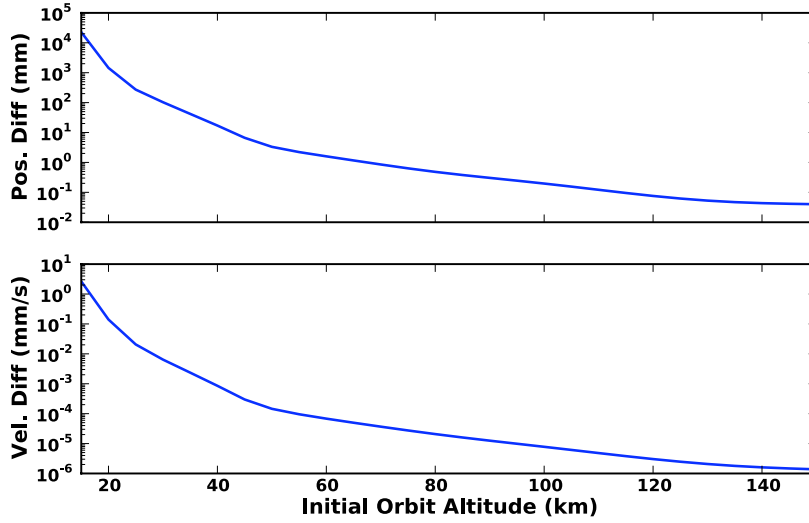
Fig. 22 Summary of 3D RMS position and velocity errors for orbits propagated with the estimated MRQSphere model versus the spherical harmonic model.

term dominates and gravity perturbations attenuate. However, a 1 m 3D RMS error is less than the 5 m orbit determination error for the NEAR mission satellite at comparable altitudes.

4 Conclusions and Future Work

In this paper, we defined the MRQSphere model and provided its example representing the gravity field of the asteroid 433 Eros. We used this example to describe performance of the model in the idealized situation. The construction of the MRQSphere model is dependent on several user-defined tuning parameters, most notably the accuracy of the Gaussian approximation of inverse powers of distance ρ. This approximation allows for the multiresolution representation of the gravity field and leads to the definition of the shells to account for its angular variations. Other presented results include the derivation of the acceleration vector and the variational equations within the MRQSphere model.

This paper also demonstrated the estimation capabilities of the MRQSphere gravity representation for a small body using measurements of the gravity potential. We have presented a systematic method for estimating the gravity field using a multiresolution representation. Given an initial gravity model, each shell of the MRQSphere model is estimated separately as the satellite slowly approaches the primary body. As information on the total gravity field improves, a redistribution algorithm applies corrections to previously estimated shells. Using measurements with relatively low accuracy and relatively good spatial distribution, a MRQSphere

model was estimated with accuracies comparable to the measurements provided. Like the spherical harmonics model, large regions without measurements yielded a reduced accuracy in the total gravity field.

The two major goals for future work are: (1) integrating the MRQSphere model with a more traditional orbit determination scheme using a SRIF, and (2) altering the representation for evaluation within the circumscribing sphere. Integration of the model with the SRIF would further demonstrate the MRQSphere's applicability to small-body gravity estimation and provide a more realistic characterization of the model's estimation capabilities using radio science observations. A challenge in this task is defining an algorithm to correct the estimation error covariance matrix using the redistribution algorithm. Research to allow for evaluation of the MRQSphere determined gravity field within the circumscribing sphere is ongoing.

A Acceleration Vector and the Variational Equations

Since the MRQSphere model is semi-analytic, we take the derivatives of Eqs. 6 and 21 to solve for the gradient, and thus the acceleration vector. We express the coordinates of the system in Cartesian coordinates where

$$\mathbf{r} = [\ x,\ y,\ z\ ]^T \tag{45}$$

and the angles ϕ and λ are represented by the unit vector $\hat{\mathbf{r}}$. Starting with Eq. 21,

$$\frac{\partial \tilde{U}}{\partial \mathbf{r}} = \frac{\mu}{R} \sum_{j \in \mathbb{Z}} \left[Z_j(\hat{\mathbf{r}}) \frac{\partial}{\partial \mathbf{r}} \left(e^{-(\ln \rho)^2 \sigma_j^2/2} \right) + e^{-(\ln \rho)^2 \sigma_j^2/2} \frac{\partial Z_j(\hat{\mathbf{r}})}{\partial \mathbf{r}} \right]. \tag{46}$$

Solving for the first partial derivative in the right hand side with $\rho = r/R$,

$$\frac{\partial}{\partial \mathbf{r}} \left(e^{-(\ln \rho)^2 \sigma_j^2/2} \right) = -e^{-(\ln \rho)^2 \sigma_j^2/2} \frac{\sigma_j^2}{2} \frac{\partial (\ln \rho)^2}{\partial \mathbf{r}}$$

$$= -e^{-(\ln \rho)^2 \sigma_j^2/2} \left(\frac{\sigma_j^2 \ln \rho}{r^2} \right) \mathbf{r}. \tag{47}$$

Upon differentiating $Z_j(\hat{\mathbf{r}})$ in Eq. 24,

$$\frac{\partial Z_j(\hat{\mathbf{r}})}{\partial \mathbf{r}} = \frac{\partial}{\partial \mathbf{r}} \left(\sum_{l=1}^{M} K_N(\hat{\mathbf{r}} \cdot \boldsymbol{\alpha}_l) w_l Z_j(\boldsymbol{\alpha}_l) \right)$$

$$= \sum_{l=1}^{M} w_l Z_j(\boldsymbol{\alpha}_l) \frac{\partial K_N(\hat{\mathbf{r}} \cdot \boldsymbol{\alpha}_l)}{\partial (\hat{\mathbf{r}} \cdot \boldsymbol{\alpha}_l)} \frac{\partial (\hat{\mathbf{r}}^T \boldsymbol{\alpha}_l)}{\partial \mathbf{r}}$$

$$= \sum_{l=1}^{M} w_l Z_j(\boldsymbol{\alpha}_l) \frac{\partial K_N(\gamma)}{\partial \gamma} \left(\left[\frac{\partial \hat{\mathbf{r}}}{\partial \mathbf{r}} \right]^T \boldsymbol{\alpha}_l \right) \tag{48}$$

where $\gamma = \hat{\mathbf{r}} \cdot \boldsymbol{\alpha}_l$. Finally, differentiating Eqs. 7, 10, 11, and 12 yields

$$\frac{\partial K_n(\gamma)}{\partial \gamma} = \frac{n+1}{4\pi} \frac{\partial \bar{K}_n(\gamma)}{\partial \gamma} \tag{49}$$

where

$$\frac{\partial \bar{K}_n(\gamma)}{\partial \gamma} = c_1 \bar{K}_{n-1}(\gamma) + \left(c_1 \gamma + \frac{1}{c_0} \right) \frac{\partial \bar{K}_{n-1}(\gamma)}{\partial \gamma} - c_2 \frac{\partial \bar{K}_{n-2}(\gamma)}{\partial \gamma} \tag{50}$$

with

$$\frac{\partial \bar{K}_0(\gamma)}{\partial \gamma} = 0 \tag{51}$$

$$\frac{\partial \bar{K}_1(\gamma)}{\partial \gamma} = \frac{3}{2}. \tag{52}$$

The resulting acceleration vector, with terms expressed using matrix operations, is

$$\ddot{\mathbf{r}} = \nabla \tilde{U}$$
$$= \frac{\mu}{R} \sum_{j \in \mathbb{Z}} e^{-(\ln \rho)^2 \sigma_j^2 / 2} \left[\left(-\frac{\sigma_j^2}{r^2} (\ln \rho) Z_j(\hat{\mathbf{r}}) \right) \mathbf{r} + \left(\frac{\partial \hat{\mathbf{r}}}{\partial \mathbf{r}} \right) \left(\sum_{l=1}^{M} w_l Z_j(\boldsymbol{\alpha}_l) \frac{\partial K_N(\gamma)}{\partial \gamma} \boldsymbol{\alpha}_l \right) \right] \tag{53}$$

where

$$\frac{\partial \hat{\mathbf{r}}}{\partial \mathbf{r}} = \left(\frac{\partial \hat{\mathbf{r}}}{\partial \mathbf{r}} \right)^T = \frac{1}{r} \mathbb{I}_{3 \times 3} - \frac{\mathbf{r} \mathbf{r}^T}{r^3}. \tag{54}$$

To facilitate future integration of the MRQSphere model with the orbit determination process, and to evaluate the Laplacian ($\nabla^2 \tilde{U}$), we solve for the Jacobian of the acceleration vector with respect to the state. This Jacobian is also the second derivative of $\tilde{U}$ with respect to the satellite position. These are often referred to as the variational equations.

We begin by solving for the second partial derivative of Eq. 21,

$$\frac{\partial^2 \tilde{U}}{\partial \mathbf{r}^2} = \frac{\mu}{R} \sum_{j \in \mathbb{Z}} \left[Z_j(\hat{\mathbf{r}}) \frac{\partial^2}{\partial \mathbf{r}^2} \left(e^{-(\ln \rho)^2 \sigma_j^2 / 2} \right) \right.$$
$$+ 2 \frac{\partial}{\partial \mathbf{r}} \left(e^{-(\ln \rho)^2 \sigma_j^2 / 2} \right) \left(\frac{\partial Z_j(\hat{\mathbf{r}})}{\partial \mathbf{r}} \right)^T$$
$$\left. + e^{-(\ln \rho)^2 \sigma_j^2 / 2} \frac{\partial^2 Z_j(\hat{\mathbf{r}})}{\partial \mathbf{r}^2} \right]. \tag{55}$$

The first derivatives were previously provided in Eqs. 47 and 48. After taking the second derivative of the exponential,

$$\frac{\partial^2}{\partial \mathbf{r}^2} e^{-(\ln \rho)^2 \sigma_j^2 / 2} = \frac{\sigma_j^2}{r^2} e^{-(\ln \rho)^2 \sigma_j^2 / 2} \left(\frac{2 \ln \rho + \sigma_j^2 (\ln \rho)^2 - 1}{r^2} \mathbf{r} \mathbf{r}^T - (\ln \rho) \mathbb{I}_{3 \times 3} \right). \tag{56}$$

The derivative of Eq. 48 is then

$$\frac{\partial^2 Z_j(\hat{\mathbf{r}})}{\partial \mathbf{r}^2} = \sum_{l=1}^{M} w_l Z_j(\boldsymbol{\alpha}_l) \left(\frac{\partial K_N(\gamma)}{\partial \gamma} \begin{bmatrix} \boldsymbol{\alpha}_l^T \frac{\partial}{\partial \mathbf{r}} \left(\frac{\partial \hat{\mathbf{r}}}{\partial x} \right) \\ \boldsymbol{\alpha}_l^T \frac{\partial}{\partial \mathbf{r}} \left(\frac{\partial \hat{\mathbf{r}}}{\partial y} \right) \\ \boldsymbol{\alpha}_l^T \frac{\partial}{\partial \mathbf{r}} \left(\frac{\partial \hat{\mathbf{r}}}{\partial z} \right) \end{bmatrix} + \frac{\partial^2 K_N(\gamma)}{\partial \gamma^2} \left[\frac{\partial \hat{\mathbf{r}}}{\partial \mathbf{r}} \boldsymbol{\alpha}_l \right] \left[\frac{\partial \hat{\mathbf{r}}}{\partial \mathbf{r}} \boldsymbol{\alpha}_l \right]^T \right) \tag{57}$$

where

$$\frac{\partial^2 K_n(\gamma)}{\partial \gamma^2} = \frac{n+1}{4\pi} \frac{\partial^2 \bar{K}_n(\gamma)}{\partial \gamma^2}, \tag{58}$$

$$\frac{\partial^2 \bar{K}_n(\gamma)}{\partial \gamma^2} = 2c_1 \frac{\partial \bar{K}_{n-1}(\gamma)}{\partial \gamma} + \left(c_1 \gamma + \frac{1}{c_0} \right) \frac{\partial^2 \bar{K}_{n-1}(\gamma)}{\partial \gamma^2} - c_2 \frac{\partial^2 \bar{K}_{n-2}(\gamma)}{\partial \gamma^2}, \tag{59}$$

and

$$\frac{\partial^2 \bar{K}_0(\gamma)}{\partial \gamma^2} = \frac{\partial^2 \bar{K}_1(\gamma)}{\partial \gamma^2} = 0. \tag{60}$$

The $\partial \hat{\mathbf{r}} / \partial x$, $\partial \hat{\mathbf{r}} / \partial y$, and $\partial \hat{\mathbf{r}} / \partial z$ terms refer to the first, second, and third column, respectively, of the matrix provided by Eq. 54. Thus, we have the variational equations, expressed in a slightly more compact form,

$$\frac{\partial^2 \tilde{U}}{\partial \mathbf{r}^2} = \frac{\mu}{R} \sum_{j \in \mathbb{Z}} e^{-(\ln \rho)^2 \sigma_j^2 / 2} \left\{ \frac{Z_j(\hat{\mathbf{r}}) \sigma_j^2}{r^2} \left(\frac{2 \ln \rho + \sigma_j^2 (\ln \rho)^2 - 1}{r^2} \mathbf{r} \mathbf{r}^T - (\ln \rho) \mathbb{I}_{3 \times 3} \right) \right.$$
$$\left. - \left(\frac{2 \sigma_j^2 \ln \rho}{r^2} \right) \mathbf{r} \left(\frac{\partial Z_j(\hat{\mathbf{r}})}{\partial \mathbf{r}} \right)^T + \frac{\partial^2 Z_j(\hat{\mathbf{r}})}{\partial \mathbf{r}^2} \right\}. \tag{61}$$

References

Ahn KS (1996) Application of singular value decomposition to gravity field model development using satellite data. PhD thesis, The University of Texas at Austin

Ahrens C, Beylkin G (2009) Rotationally invariant quadratures for the sphere. Proceedings of the Royal Society A 465(2110):3103–3125

Augustine NR, Austin WM, Chyba C, Kennel CF, Bejmuk BI, Crawley EF, Lyles LL, Chiao L, Greason J, Ride SK (2009) Seeking a human spaceflight program worthy of a great nation. Tech. rep., U.S. Human Spaceflight Plans Committee

Beylkin G, Cramer R (2002) Toward multiresolution estimation and efficient representation of gravitational fields. Celestial Mechanics and Dynamical Astronomy 84:87–104

Beylkin G, Monzón L (2010) Approximation by exponential sums revisited. Applied Computational Harmonic Analysis 28(2):131–149

Cheng AF, Santo AG, Heeres KJ, Landshof JA, Farquhar RW, Gold RE, Leet SC (1997) Near-Earth Asteroid Rendezvous: Mission overview. Journal of Geophysical Research 102(E10):23,695–23,708

Fehlberg E (1968) Classical fifth-, sixth-, seventh-, and eight-order Runge-Kutta formulas with stepsize control. Technical Report NASA-TR-R-287, NASA Marshall Space Flight Center, Huntsville, Alabama

Fujiwara A, Mukai T, Kawaguchi J, Uesugi KT (2000) Sample return mission to NEA: MUSES-C. Advances in Space Research 25(2):231–238

Garmier R, Barriot JP, Konopliv AS, Yeomans DK (2002) Modeling of the Eros gravity field as an ellipsoidal harmonic expansion from the near doppler tracking data. Geophysical Research Letters 29(8):721–723

Glassmeier KH, Boehnhardt H, Koschny D, Kührt E, Richter I (2007) The Rosetta mission: Flying towards the origin of the solar system. Space Science Reviews 128(1-4):1–21

Gradshteyn IS, Ryzhik IM (2007) Table of Integrals, Series and Products, 7th edn. Elsevier Academic Press

Jones BA, Born GH, Beylkin G (2010) Comparisons of the cubed-sphere gravity model with the spherical harmonics. Journal of Guidance, Control, and Dynamics 33(2):415–425

Konopliv AS, Asmar SW, Carranza E, Sjogren W, Yuan D (2001) Recent gravity models as a result of the Lunar Prospector mission. Icarus 150(1):1–18

Konopliv AS, Miller JK, Owen WM, Yeomans DK, Giorgini JD (2002) A global solution for the gravity field, rotation, landmarks, and ephemeris of Eros. Icarus 160:289–299

Marov MY, Avduevsky VS, Akim EL, Eneev TM, Kremnev RS, Kulikov SD, Pichkhadze KM, Popov GA, Rogovsky GN (2004) Phobos-Grunt: Russian sample return mission. Advances in Space Research 33(12):2276–2280

Russell CT, Coradini A, Christensen U, Sanctis MCD, Feldman WC, Jaumann R, Keller HU, Konopliv AS, McCord TB, McFadden LA, McSween HY, Mottola S, Neukum G, Pieters CM, Prettyman TH, Raymond CA, Smith DE, Sykes MV, Williams BG, Wise J, Zuber MT (2004) Dawn: A journey in space and time. Planetary and Space Science 52(5-6):465–489

Scheeres DJ (2002) The orbital dynamics environment of 433 Eros. In: 23rd International Symposium on Space Technology and Science, Matsue, Japan

Szegö G (1975) Orthogonal Polynomials, 4th edn. American Mathematical Society, Providence, RI

Takahashi Y, Scheeres DJ (2010) Rapid characterization of a small body via slow flybys. In: 20th Annual AAS/AIAA Spaceflight Mechanics Meeting, San Diego, California

Tapley BD, Schutz BE, Born GH (2004) Statistical Orbit Determination, 1st edn. Elsevier Academic Press, Burlington, MA

Tsoulis D, Jamet O, Verdun J, Gonindard N (2009) Recursive algorithms for the computation of the potential harmonic coefficients of a constant density polyhedron. Journal of Geodesy 83(10):925–942

Zuber MT, Smith DE, Cheng AF, Garvin JB, Aharonson O, Cole TD, Dunn PJ, Guo T,
    Lemoine FG, Neumann GA, Rowlands DD, Torrence MH (2000) The shape of 433 Eros
    from the NEAR-Shoemaker laser rangefinder. Science 289:2091–2101